Interannual polar vortex–ozone co-variability

Frederik Harzer[1], Hella Garny[2,1], Felix Ploeger[3,4], Harald Bönisch[5], Peter Hoor[6], and Thomas Birner[1,2]

[1]Ludwig-Maximilians-Universität, Meteorological Institute, Munich, Germany
[2]Deutsches Zentrum für Luft- und Raumfahrt, Institute of Atmospheric Physics, Oberpfaffenhofen, Germany
[3]Forschungszentrum Jülich, Institute of Energy and Climate Research, Stratosphere (IEK-7), Jülich, Germany
[4]University of Wuppertal, Institute for Atmospheric and Environmental Research, Wuppertal, Germany
[5]Karlsruhe Institute of Technology, Institute of Meteorology and Climate Research, Karlsruhe, Germany
[6]Johannes Gutenberg University, Institute for Atmospheric Physics, Mainz, Germany

Correspondence: Frederik Harzer (frederik.harzer@physik.lmu.de)

Abstract. Stratospheric ozone is important for both stratospheric and surface climate. In the lower stratosphere during winter its variability is governed primarily by transport dynamics induced by wave-mean flow interactions. Here, we focus on interannual co-variations between the zonal mean ozone distribution and the strength of the polar vortex during northern hemispheric winter. Specifically, we study co-variability between the seasonal means of the ozone field from modern reanalyses and polar cap-averaged temperature at 100 hPa, which represents a robust and well-defined index for polar vortex strength. We consider variability in both pressure and isentropic coordinates. In the former case, we find that anomalously weak polar vortex years are associated with increased polar ozone amounts, showing two pronounced local maxima: one in the lower to mid-stratosphere and one just above the polar tropopause. In contrast, in isentropic coordinates, only the mid- to lower stratosphere shows increased ozone, while a small negative ozone anomaly appears in the lowermost stratosphere. These differences are related to contributions due to anomalous adiabatic vertical motion, which are implicit in potential temperature coordinates. In general, our analyses of the ozone budget in the extratropical middle stratosphere show that interannual polar ozone variability can be explained by a combination of anomalous diabatic downwelling and quasi-isentropic eddy mixing that are associated with consecutive, counteracting anomalous ozone tendencies on daily time scales. We find that approx. 71 % of the total variability of polar column ozone in the stratosphere is associated with year-by-year variations in polar vortex strength based on ERA5 reanalyses for the winter seasons 1980–2022. MLS observations for 2005–2020 show that around 86 % can be explained by polar vortex co-variability.

1 Introduction

Atmospheric ozone has manifold effects on human health and ecosystems on earth (e. g., Barnes et al., 2022). Furthermore, ozone is known to contribute to climate feedbacks due to its radiative properties (WMO, 2018, 2022; IPCC, 2021), emphasizing its relevance for atmospheric and climate sciences. For example, Arctic ozone variability was found to substantially impact tropospheric and surface climate (Smith and Polvani, 2014; Calvo et al., 2015; Ivy et al., 2017; Friedel et al., 2022a, b). Diagnostics based on Antarctic ozone depletion have been proposed to improve seasonal forecasts due to robust correlations with the southern annular mode (Son et al., 2013; Bandoro et al., 2014). Moreover, recent studies reported significant effects of
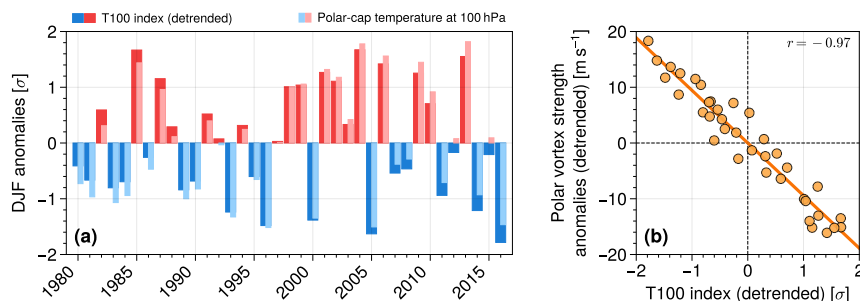
Figure 1. (a) T100 index obtained from ERAI reanalysis data, adjusted for a linear trend in time as required for the linear regression approach. The underlying polar-cap averaged temperature anomalies at the 100 hPa level, without this trend removed, are shown by the thin bars. Both time series are standardized by the standard deviation of the T100 index, $\sigma = 2.6\,\text{K}$. **(b)** Interannual anomalies of the zonal mean zonal wind at the polar vortex around 60°N and 10 hPa, regressed on the T100 index with regression coefficient $b = -9.4\,\text{m}\,\text{s}^{-1}\,\sigma^{-1}$ and correlation $r = -0.97$. All results are for ERAI, DJF 1979/80–2015/16.

CO$_2$-induced ozone changes on climate sensitivity and on the tropospheric circulation based on models that include interactive

25 ozone (Dietmüller et al., 2014; Nowack et al., 2015, 2018; Chiodo and Polvani, 2017, 2019; Chiodo et al., 2018).

During northern hemispheric winters, major dynamical variability is due to variations of the strength of the stratospheric polar vortex. The associated, significant anomalies of ozone in the lower stratosphere, where ozone is regulated primarily through transport processes, have been studied extensively (e. g., de la Cámara et al., 2018a, b; Lawrence et al., 2020; Oehrlein et al., 2020; Hong and Reichler, 2021; Bahramvash Shams et al., 2022). They have been found to greatly affect transport

30 of stratospheric ozone into the troposphere, which is modulated by the amount of ozone that is available in the lowermost stratosphere (Holton et al., 1995; Gettelman et al., 2011; Neu et al., 2014; Albers et al., 2018; Wang and Fu, 2021).

In this work, we study intrinsic climate variability by considering interannual zonal mean ozone anomalies during northern hemispheric winters. Therefore, we apply a simple linear regression approach to investigate co-variability with the seasonal strength of the polar vortex. We focus on variations in the polar stratosphere, which are expected to be governed mainly by the

35 Brewer–Dobson circulation, coupled to the variability of polar vortex strength. We find that the resulting winter-mean ozone response pattern may be explained by combined effects of both mixing and residual circulation transport.

This paper is structured as follows. In Sect. 2, we list the data used for this study and discuss the setup for the linear regressions. The resulting ozone response signatures are analysed in Sect. 3 for both pressure and potential temperature coordinates. In Sect. 4, we perform an ozone budget analysis to shed light on the dynamical ozone transport processes associated with the

40 variability of polar vortex strength. Section 5 summarizes our results and provides a brief outlook.
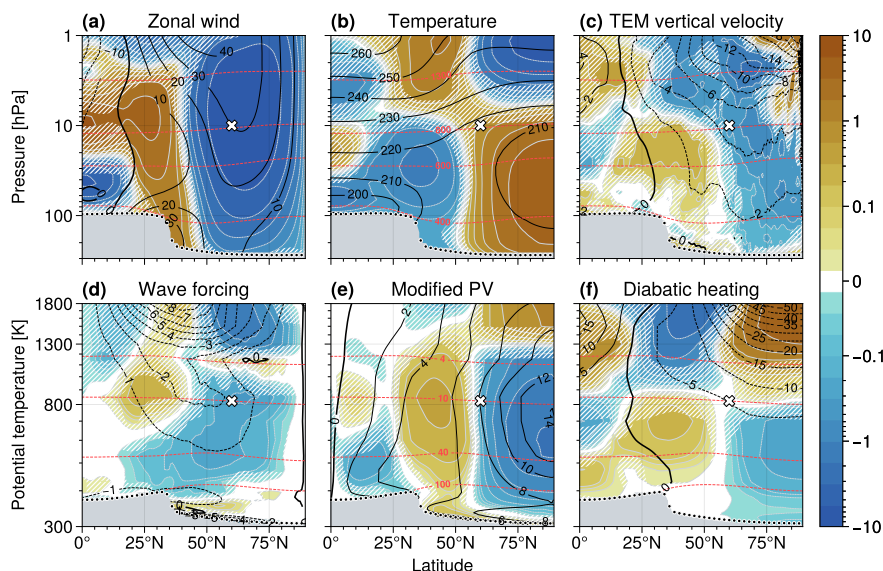
Figure 2. Interannual anomalies of the zonal mean **(a)** zonal wind (in units of $m\,s^{-1}$), **(b)** temperature (K), **(c)** TEM vertical velocity in log-p coordinates ($km\,month^{-1}$), i. e., $W_r = -(H/p)\,\omega_r$ with scale height $H = 7\,km$ and ω_r from eq. (3), **(d)** PV flux $\overline{\hat{v}\sigma\hat{q}}\cos\phi$ (in $m\,s^{-1}\,day^{-1}$) as a diagnostic for adiabatic wave forcing (Tung, 1986), **(e)** modified PV $\overline{\Pi}^* \equiv \overline{q}^* (\theta/\theta_0)^{-9/2}$ in units of $1\,PVU = 1 \times 10^{-6}\,K\,m^2\,kg^{-1}\,s^{-1}$ (Lait, 1994), with density-weighted PV $\overline{q}^*$ and $\theta_0 = 350\,K$, and **(f)** diabatic heating $\overline{Q}^*$ ($K\,day^{-1}$), regressed on the standardized ERAI T100 index. The regression maps are visualized by the color shading and measured per one standard deviation of the index. Note that the panels in the first and second row show the results for pressure and isentropic coordinates, respectively. Hatches indicate where the regressions are not statistically significant. Contour lines show the DJF climatologies of the input fields. The approximate position of the polar vortex around 60°N and 10 hPa is shown by the white markers. The thick dotted lines represent the mean thermal tropopause for DJF.[1] Red dashed lines show selected isentropes (in K, top row) and isobars (in hPa, bottom row), respectively. Note uneven color contour intervals with linear spacing for values within ± 0.1 and logarithmic spacing outside that range. All results are based on ERAI, DJF 1980–2016.

2 Data and methods

For the main part of this study, we use model level output of ERA-Interim reanalyses (Dee et al., 2011) for 1979–2016, which we interpolated on pressure and potential temperature levels such that the full vertical resolution of the model was preserved. With that, we consider zonal-mean data on both pressure and isentropic levels on a vertical range roughly from 1000 hPa to 1 hPa and 260 K to 1800 K, respectively, with a meridional resolution of about 0.7°. Monthly means are derived from 6-hourly daily data and are combined for seasonally averaged fields for December–February (DJF) 1980–2016. We will refer to the year of January for labeling the corresponding winter season.

Detailed assessments show that ERA-Interim (ERAI) ozone in the lower stratosphere is in reasonable agreement with observations and other reanalysis products (Dragani, 2011; Albers et al., 2018; Davis et al., 2022). We intend to provide further

---

[1] Throughout this study, thermal tropopause heights are calculated using PyTropD (Adam et al., 2018), following the definition by WMO (1957).

50   validation by comparing our results obtained from ERAI on pressure levels with those based on the latest ERA5 reanalyses for DJF 1960–2022 with regular 1.5° meridional grid spacing (Hersbach et al., 2019, 2020; Bell et al., 2021). ERA5 data for the pre-satellite era, covering DJF 1960–1980, will be evaluated separately. In addition, we use ozone observations from the Microwave Limb Sounder (MLS) instrument on board the Aura satellite, data version 5 (Waters et al., 2006; Livesey et al., 2022). The spatial sampling of MLS is comparatively high, with about 3500 profiles along about 15 orbits per day, covering the

55   globe between about 82°S and 82°N. The MLS profile data has been interpolated on potential temperature levels and monthly mean zonal mean climatologies have been compiled for both pressure and potential temperature levels. In this paper, MLS data is considered on pressure levels for DJF 2005–2020 on a non-regular latitudinal grid with mean resolution of approx. 4.2°.

    Throughout this study, correlations are measured by local Pearson correlation coefficients r and p-values are calculated by a two-sided Wald t-test. Statistical significance is assumed if $p \leq 0.05$. 95 % confidence intervals for the correlation coefficients

60   are computed based on Fisher's z-transformation.

    Co-variability between stratospheric ozone and polar vortex strength is studied by using a simple linear least-squares regression model: first, we define an index time series that is derived from interannual zonal mean temperature, interpolated at the 100 hPa pressure level and averaged over the Northern Hemisphere's polar cap,

$$\overline{T}_{100}(t) \equiv \left\langle \overline{T}(t, p = 100\,\mathrm{hPa}, \phi) \right\rangle_{\phi \geq 60°\mathrm{N}}, \tag{1}$$

65   which we will refer to as "T100 index" in the following. Here, overbars indicate the zonal mean and squared brackets denote meridional averaging. The relation between the T100 index and polar vortex strength variability is discussed below within the context of atmospheric dynamics. Then, for a given variable field $\overline{y}$, the corresponding anomalies $\delta\overline{y}$ are regressed on this index according to

$$\delta\overline{y}(t) = a + b \cdot \overline{T}_{100}(t) + \epsilon(t). \tag{2}$$

70   For both the index and the anomaly time series, potential linear trends across the whole time range under consideration are identified through separate linear least-squares regressions and removed beforehand. Finally, the set of regression coefficients $b(p, \phi)$ yields a "T100 regression map" across the latitude-height plane that quantifies the statistical linear response of $\overline{y}$ if polar stratospheric temperature, measured by the standardized T100 index, is varied by one standard deviation. In this work, this regression model is primarily applied to zonal mean year-by-year anomalies covering DJF winter seasons on the

75   Northern Hemisphere. When daily anomalies are considered, the procedure is similar except that in addition the time series are deseasonalized beforehand.

    The detrended and standardized T100 index derived from ERAI reanalyses for DJF 1980–2016 is provided in Fig. 1(a). Choosing this T100 predictor for studying polar vortex co-variability is justified due to its strong dependence on variations of the zonal wind in the polar vortex region at 60°N and 10 hPa, as shown in Fig. 1(b). We therefore obtained a well-defined and

80   powerful proxy diagnostic for the strength of the polar vortex during northern hemispheric winters. Based on temperature as a fundamentally constrained variable instead of zonal wind, this definition features a robust T100 time series across selected other reanalysis products and for moderate changes of the pressure level at which this index is evaluated (not shown).
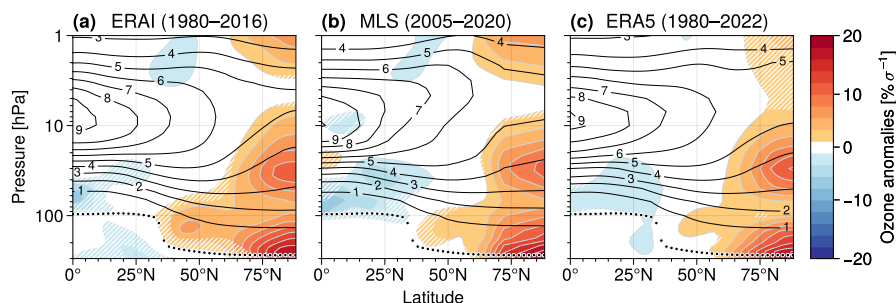
Figure 3. Interannual zonal mean ozone on pressure levels from **(a)** ERAI (DJF 1980–2016), **(b)** MLS (2005–2020) and **(c)** ERA5 (1980–2022), regressed on the standardized ERA5 T100 index. The response signatures are provided as relative anomalies (in $\% \, \sigma^{-1}$) based on the respective ozone DJF climatology that is shown by the black contour lines each (in ppmv). The thick dotted lines show the mean thermal tropopause for DJF, derived from ERAI. Other details as in Fig. 2.

The strength of the polar vortex and polar-cap lower stratospheric temperature are coupled via downward control (Haynes et al., 1991). Some important variable fields, which are intended to illustrate this mechanism, and their T100 regression maps are provided in Fig. 2. Briefly, starting with anomalously strong wave activity of tropospheric origin, westerly winds in the polar vortex region are reduced (as shown in Fig. 2a) upon enhanced wave dissipation, inducing a wave-driven poleward residual flow that counteracts the weakening of the background zonal wind due to the Coriolis effect. The wave forcing is indicated by enhanced equatorward potential vorticity (PV) fluxes around the 800 K isentrope in Fig. 2(d) that reduce PV above the polar cap (Fig. 2e). The associated temperature response in Fig. 2(b) is consistent with thermal wind balance. Downwelling (upwelling) is associated with adiabatic warming (cooling), such that by continuity this closes the anomalous residual circulation. This vertical motion (shown with log-p scaling in Fig. 2c) is captured in the Transformed Eulerian Mean (TEM) framework by (e. g., Andrews et al., 1987)

$$\overline{\omega}_{\mathrm{r}} = \overline{\omega} + \frac{1}{a \cos\phi \, \partial_p \overline{\theta}} \partial_\phi \left(\overline{v'\theta'} \cos\phi \right), \tag{3}$$

where $\overline{\omega} = \mathrm{d}p/\mathrm{d}t$ is the vertical velocity in pressure coordinates, $\overline{\theta}$ denotes zonal mean potential temperature, $\overline{v'\theta'}$ indicates the meridional eddy heat transport and a is the earth's radius. The change in potential temperature due to diabatic heating in Fig. 2(f) can be consistently explained to damp the wave-driven temperature perturbations through radiative cooling.

The underlying mechanism has been widely discussed in studies on stratosphere–troposphere coupling, where also the T100 index described above has been first introduced (Baldwin et al., 2019; Domeisen et al., 2020). On sub-seasonal time scales, similar effects are observed, e. g., during sudden stratospheric warmings (Butler et al., 2017; Baldwin et al., 2021).

3 Polar vortex–ozone co-variability: T100 response signatures

In the lower stratosphere, it is mainly the Brewer–Dobson circulation (BDC) that captures ozone transport from the tropics towards higher latitudes (Gettelman et al., 2011; Butchart, 2014). Since wave forcing impacts the strength of both the polar
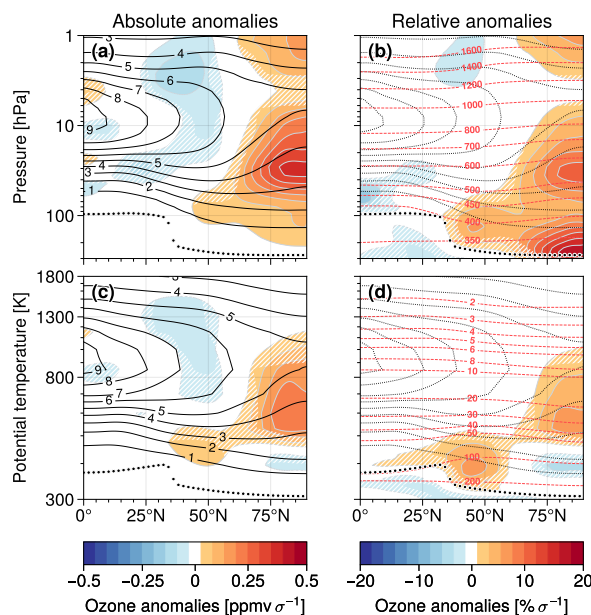
Figure 4. (a) T100 regression map for anomalous zonal mean ozone $\overline{\chi}$ on pressure levels (ERAI, DJF 1980–2016). **(b)** Same as in **(a)** but the response signature is given by relative anomalies with respect to the DJF ozone climatology. **(c, d)** Corresponding T100 regression maps for density-weighted zonal mean ozone on potential temperature levels, $\overline{\chi}^* = \overline{\rho_\theta \chi}/\overline{\rho_\theta}$ where ρ_θ is isentropic density. Details as in Fig. 3.

vortex and the BDC, an anomalously weak polar vortex tends to be associated with enhanced poleward ozone transport and, hence, increased polar ozone amounts. Since previous studies reported a strong coupling between the strength of the BDC

105 and stratospheric temperature (Fu et al., 2010; Weber et al., 2011; Young et al., 2012), this suggests substantial interannual co-variability between the T100 diagnostic and stratospheric ozone. In this section, we aim to document this ozone variability based on two different coordinate perspectives.

Figure 3 shows zonal mean ozone volume mixing ratios $\overline{\chi}$ both from ERAI and ERA5 reanalysis data as well as from MLS observations, regressed on the standardized ERA5 T100 index that represents an extended (available for DJF 1980–

110 2022) but essentially equivalent version of the ERAI T100 time series due to its outstanding high correlation, $r > 0.99$. The regression maps are provided in relative units, based on the corresponding ozone DJF climatology, and per one standard deviation of the T100 index. The stratospheric response signatures show very good agreement among the different datasets. From a more detailed analysis, robust results were found for selected other reanalysis products and for modern chemistry–climate models (not shown; see also von Heydebrand, 2022).

115 In general, Fig. 3 supports the idea that higher ozone amounts over the polar cap are related to anomalously strong poleward transport due to a stronger BDC during weak polar vortex years. However, the vertical structure of the polar ozone anomalies may be more surprising: of particular interest are the two pronounced response maxima in the mid- to lower polar stratosphere

and just above the polar tropopause, as well as another spot of enhanced ozone in the mid-latitudes for each of the three datasets evaluated in Fig. 3.

120   For understanding these features, we can retrieve some first insights from just evaluating the differences among the response signatures obtained for pressure and potential temperature as the vertical coordinate. For that, consider Fig. 4 which shows the T100 regression maps for zonal mean ozone $\overline{\chi}$ on pressure levels (top row) and density-weighted ozone, $\overline{\chi}^* = \overline{\rho_\theta \chi}/\overline{\rho_\theta}$ with isentropic density $\rho_\theta = g^{-1}\partial_\theta p$, for potential temperature coordinates (bottom row), both obtained from ERAI reanalysis data for DJF 1980–2016. For comparison, the response signatures are displayed not only in relative units (right column) but also as

125   absolute anomalies in parts-per-million (left column), $1\,\mathrm{ppmv} = 1 \times 10^{-6}\,\mathrm{mol\,mol^{-1}}$.

    The results show clear differences among the two coordinate frameworks, which shed light on some relevant transport processes that build up this ozone response signature. For example, consider the two upper polar response maxima around $1\,\mathrm{hPa}$ and $30\,\mathrm{hPa}$, respectively, and the corresponding minima at similar altitudes around 40°N more pronounced in the absolute anomalies (top row in Fig. 4). We expect them to arise due to the quadrupole-like response in temperature and TEM vertical

130 velocity (Figs. 2b and 2c), associated with the anomalously weak polar vortex in Fig. 2(a). The sign of the ozone response directly follows from the anomalous up- and downwelling acting on the local vertical gradient of the background ozone distribution. In contrast, this response is much weaker in potential temperature coordinates (bottom row in Fig. 4). This is because vertical ozone transport includes a component due to adiabatic motion which satisfies $\mathrm{d}\theta/\mathrm{d}t = 0$ and can be thought of shifting iso-surfaces of both ozone and potential temperature simultaneously. Thus for vertical transport, unlike the diabatic part, the

135 adiabatic proportion is implicitly accounted for in isentropic coordinates. Konopka et al. (2009) used similar arguments to explain differences in amplitude of the seasonal cycle of tropical ozone when viewed in pressure and isentropic coordinates.

    In the lowermost stratosphere just above the polar tropopause, we find the most remarkable differences among the results for the two coordinate systems used in Fig. 4. On pressure levels, from Fig. 4(b) we find a pronounced ozone response maximum with relative anomalies of more than $15\,\%\,\sigma^{-1}$. Using potential temperature as the vertical coordinate, we instead obtain

140 a decrease of ozone there in Fig. 4(d), suggesting that anomalous downwelling (shown in Fig. 2c) contains a much larger adiabatic component there compared with higher stratospheric regions. This is consistent with smaller radiative damping rates that are observed in the lower polar stratosphere and that limit the effectiveness of diabatic cooling (Hitchcock et al., 2010).

    The large differences between pressure and isentropic coordinates in the lowermost stratosphere are also apparent when considering variations of the polar cap tropopause (Fig. 5): tropopause pressure shows a much larger response to T100 variability

145 (by about a factor of ten) than potential temperature, indicating that polar tropopause height variability is mainly governed by adiabatic processes. Significantly enhanced ozone at the polar tropopause then is observed where the substantial lowering of the tropopause height allows for downward transport of stratospheric ozone into former tropospheric regions, which is the case for pressure rather than potential temperature coordinates.

    Taking into account comprehensive research by de la Cámara et al. (2018a, b) on anomalous stratospheric dynamics and

150 Arctic ozone during sub-seasonal sudden stratospheric warming events, we hypothesize that the remaining T100 response signatures in Figs. 3 and 4 can be explained through variations of the BDC, combining the effects of residual-mean (net mass)
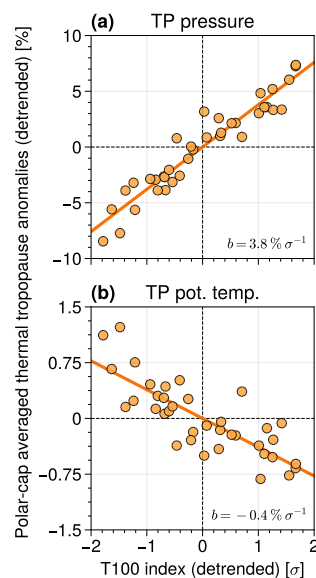
Figure 5. (a) Polar-cap averaged thermal tropopause (TP) pressure regressed on the T100 index (ERAI, DJF 1980–2016), with slope $b = 3.8\,\%\,\sigma^{-1}$ from a linear least-squares fit and correlation $r = 0.95$. Much less co-variability is found in **(b)** for polar-cap TP potential temperature ($r = -0.80$).

downwelling and quasi-isentropic eddy mixing, depending on the local gradients of stratospheric ozone. Within this context, analysing the full ozone budget turned out to be appropriate to investigate the actual roles of these transport contributions.

4 Insights on polar vortex–ozone co-variability from the ozone budget

155 Using isentropic coordinates, the zonal mean ozone budget reads (e. g., Andrews et al., 1987; Plumb, 2002)

$$\underbrace{\partial_t \overline{\chi}^* + \frac{\overline{v}^*}{a}\partial_\phi \overline{\chi}^*}_{-①} + \underbrace{\overline{Q}^*\partial_\theta \overline{\chi}^*}_{-②} = -\overline{\rho_\theta}^{-1}\left[\underbrace{\frac{1}{a\cos\phi}\partial_\phi\left(\overline{\widehat{v}\rho_\theta\widehat{\chi}}\cos\phi\right)}_{③} + \underbrace{\partial_\theta\overline{\widehat{Q}\rho_\theta\widehat{\chi}}}_{④}\right] + \overline{S}^*. \tag{4}$$

Here, χ denotes the ozone volume mixing ratio, $Q = \mathrm{d}\theta/\mathrm{d}t$ is the change in potential temperature due to diabatic heating, $\rho_\theta = g^{-1}\partial_\theta p$ is isentropic density and S represents sources and sinks. We use a density-weighted zonal average, $\overline{\chi}^* \equiv \overline{\rho_\theta\chi}/\overline{\rho_\theta}$ with $\widehat{\chi} = \overline{\chi} - \overline{\chi}^*$ indicating deviations therefrom, and spherical coordinates with geographical latitude ϕ and earth's radius 160 a. The tendencies induced by mean flow advection and by eddy mixing are accounted for by the terms ①+② and ③+④, respectively.

Figure 6 provides the T100 regression maps for the relevant dynamical fields and their associated ozone tendencies. We have neglected the contributions due to the mean meridional flow and due to vertical eddy ozone transport, numbered with ① and ④ in eq. (4), since they are small compared to the other processes (not shown). We further omit contributions to ozone 165 variability due to chemistry, i. e., $S \approx 0$ in eq. (4), which is typically fulfilled in the lower stratosphere, albeit under very
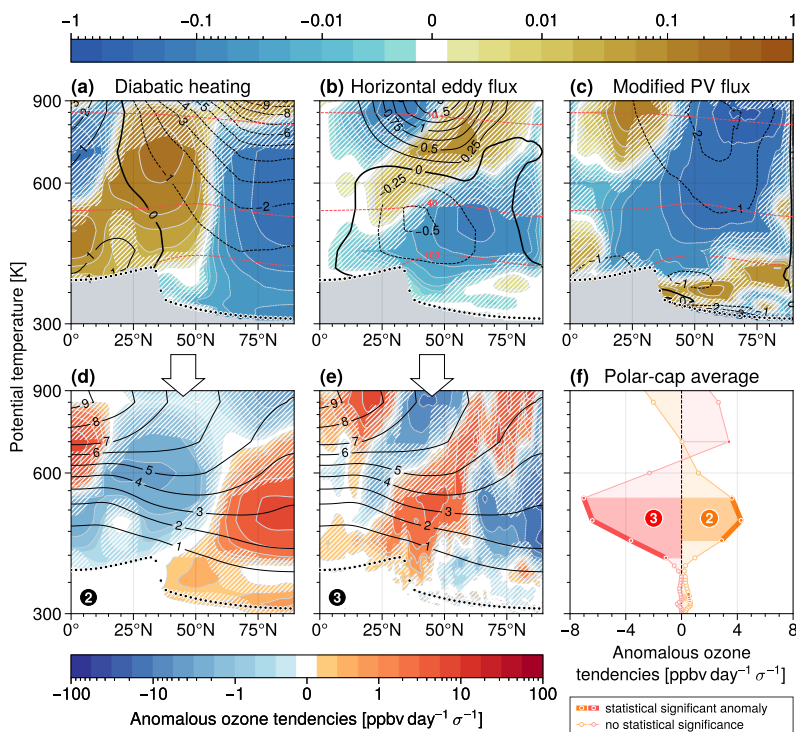
Figure 6. (a) Anomalous diabatic heating rates $\overline{Q}^{*}$ (in K day^{-1}) and (b) horizontal eddy ozone transport $\overline{\hat{v}\rho_{\theta}\hat{\chi}}/\overline{\rho_{\theta}}$ (in ppmv m s^{-1}) regressed on the T100 index (ERAI). (c) The corresponding regression map for the modified PV flux $\overline{\hat{v}\rho_{\theta}\hat{\Pi}}/\overline{\rho_{\theta}}$ (in PVU m s^{-1}) is added for comparison. Details as in Fig. 2. (d, e) T100 regression maps for the anomalous tendencies ② and ③ from eq. (4). Here, the black contours show the ozone DJF climatology (in ppmv). Note uneven color contour intervals with linear spacing for values within ±0.01 (top row) and ±1 ppbv day^{-1} σ^{-1} (bottom row), respectively, and logarithmic spacing outside those ranges. The anomalous ozone tendencies seem to be weak in the lowermost stratosphere and increase strongly for altitudes higher than 400 K due to increased wave forcing above that isentrope as indicated by the anomalous equatorward PV fluxes in (c). Weak positive ozone tendencies due to enhanced diabatic cooling directly above the tropopause in (d) probably arise from an increase in static stability there, e. g., as observed for sudden stratospheric warmings (Grise et al., 2010; Son et al., 2011; Wargan and Coy, 2016), or can be explained as a second-order feedback reacting to changes in the vertical ozone gradients. (f) Polar-cap averaged tendencies, $\langle \partial_{t}\overline{\chi}^{*}\rangle_{\phi}$ for $\phi \geq 60°$N, regressed on the ERAI T100 index. Thick solid lines mark isentropes with statistically significant anomalies. All results are for ERAI, DJF 1980–2016.

cold conditions, ozone depletion may still become important there (e. g., Brasseur and Solomon, 2005). Contributions due to chemistry cannot be neglected in the upper stratosphere; we therefore limit our budget analysis to lower-stratospheric regions, such that $\theta < 900$ K in Fig. 6.

The results show that pronounced anomalous ozone tendencies are mainly found between 400 K and 700 K, where anoma-
170 lous diabatic vertical transport above the polar cap brings ozone-rich air to lower altitudes, whereas quasi-isentropic eddy mixing counteracts that response by transporting ozone from the polar region to mid-latitudes. These two leading contributions
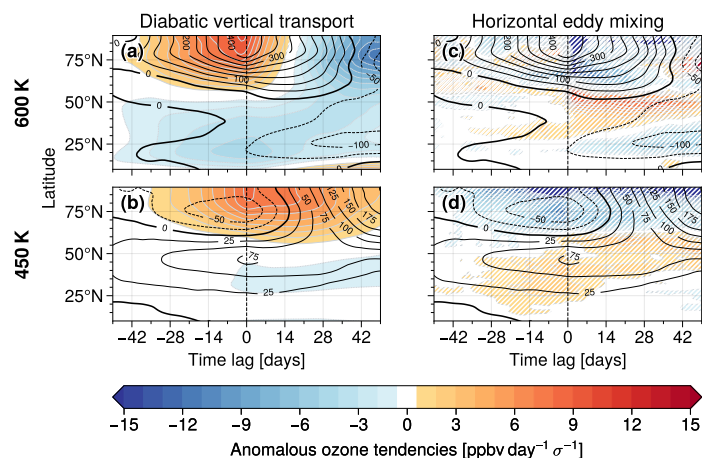
Figure 7. Anomalous ozone tendencies associated with **(a, b)** diabatic heating, ② in eq. (4), and **(c, d)** horizontal eddy mixing ③, respectively, regressed on daily T100 anomalies on the 600 K (top row) and 450 K (bottom row) isentrope. Evaluation of a robust positive response at 600 K associated with anomalous diabatic mean flow advection in the tropics (not shown), which occured across all the lag times considered here and possibly includes the response of the quasi-biennial oscillation, remains for subsequent work. Positive (negative) lag times indicate that the field anomalies succeed (precede) the T100 index. Hatching indicates where co-variability is not statistically significant. Black contour lines illustrate T100 lag regressions for daily ozone anomalies $\overline{\chi}^*$ in ppbv per standard deviation σ of the daily T100 index. All results are for deseasonalized daily-mean ERAI data, covering December, January and February months in 1979–2016.

to ozone variability, ② and ③ in Figs. 6(d) and 6(e), in large parts compensate each other, which is also illustrated by the polar-cap averaged anomalous ozone tendencies in Fig. 6(f). This is as expected, since individual seasonal averages should be in approximate steady state, hence, in principle no residual ozone tendency is expected. In fact, we did not find a robust response

175   profile for the resulting net tendency that follows from the anomalous tendencies ②+③ in Fig. 6(f), i. e., statistical significance (if any) is sensitive to the latitude range chosen for polar-cap averaging (not shown). Provided that no other relevant tendencies (especially due to ozone chemistry) need to be considered here, we conclude that in this case the full seasonal-mean ozone budget is indeed balanced, i. e., the T100 response of the net tendency $\partial_t \overline{\chi}^* \approx ② + ③$ vanishes for seasonal averages although uncertainties remain in ERAI.

180   To reveal more insights into the drivers of the seasonal-mean ozone anomalies it is useful to study daily variability where the relevant transport contributions may not fully compensate, leaving a net ozone tendency that allows to better distinguish cause and effect. To do so, we perform a linear lag-regression analysis using daily averaged fields based on 6-hourly ERAI data for the December, January and February months in 1979–2016. We select two isentropes, 450 K and 600 K, which represent the polar ozone response maximum and the minimum underneath in Fig. 4(c), and assess T100 co-variability for daily ozone

185   and the two relevant dynamical tendencies, ② and ③ in eq. (4). The results for different lag times, covering 14 weeks in total centered around the T100 anomaly, are shown in Fig. 7. For the 600 K isentrope, we find that enhanced polar ozone is mainly induced by anomalous diabatic mean flow downwelling (for negative lag times in Fig. 7a). Subsequently, a reduction of polar

ozone takes place due to increased quasi-horizontal eddy mixing in Fig. 7(c) out of the polar cap toward mid-latitudes, which partly arises as a feedback due to strenghtened meridional ozone gradients. Concerning the 450 K level, it turns out that the
190   temporal order of the tendencies involved is now reversed: here, horizontal eddy mixing can be clearly identified to force the negative ozone response in the polar region. This also explains the positive ozone anomaly in the mid-latitudes. Figures 7(a) and 7(b) indicate the anomalies in diabatic mean flow advection propagating downward with time, where they counteract the eddy forcing in lower altitudes. A closer analysis of variations in the underlying wave driving giving rise to anomalous transport, including different contributions due to different parts of the wave spectrum, is beyond the scope of the current analyses and is
195   left for future work.

Overall, our findings here suggest that the complex ozone response signature in the middle stratosphere introduced in Sect. 3 can be explained by the combined effects of horizontal eddy mixing and vertical mean flow advection. We found significant anomalous ozone tendencies as the T100 response on sub-seasonal time scales, which consistently explain the variations in seasonal-mean stratospheric ozone but at the same time do not influence the net tendencies on a seasonal scale. The key for
200   this to happen are those two dominant mechanisms of ozone transport that induce competing response tendencies but occur with some temporal distance.

5   Discussion and conclusions

Our analyses reveal the following aspects of interannual co-variability between the strength of the polar vortex and polar-cap ozone for northern hemispheric winter: in pressure coordinates, an anomalously weak vortex is associated with increased ozone
205   volume mixing ratios throughout the stratosphere, showing local maxima in the lower-to-middle stratosphere and just above the polar tropopause. Using potential temperature as the vertical coordinate, increased ozone is only present in lower altitudes roughly below 900 K, even showing weakly decreased values in the lowermost stratosphere. We rationalize these disparate ozone variations by a combination of variability in wave-driven quasi-horizontal mixing and vertical advection by the residual circulation. In particular,

210   1. wave-driven anomalous adiabatic up- and downwelling in the polar vortex region cause enhanced polar ozone around 1 hPa and 30 hPa, as well as less ozone equatorwards,

    2. increased downwelling associated with an anomalously weak polar vortex includes a large adiabatic component and acts to simultaneously shift iso-surfaces of potential temperature and ozone also in the lowermost stratosphere, which furthermore results in a lowered tropopause and significantly increased ozone concentrations there, and

215   3. the ozone response signature in the middle stratosphere can be explained by consecutive, counteracting anomalous tendencies associated with diabatic downwelling and quasi-isentropic eddy mixing on daily time scales, with varying chronological order depending on altitude.

We may therefore conclude that interannual ozone variations are governed by similar dynamical processes as sub-seasonal ozone variability (see, e. g., Lubis et al., 2017; de la Cámara et al., 2018a, b; Hong and Reichler, 2021; Bahramvash Shams
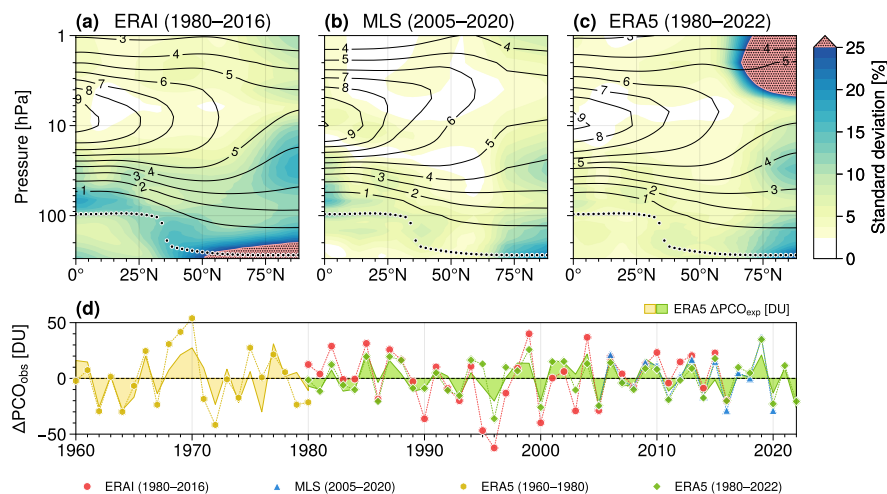
Figure 8. (a–c) Maps of interannual ozone variability, based on local sample standard deviations relative to the ozone DJF climatology, for ERAI, MLS and ERA5. The thick dotted lines show the mean thermal tropopause derived from ERAI data. For ERAI and ERA5, extreme ozone variations (indicated by red shading and stippling) are caused by statistical outliers. **(d)** Observed polar-cap averaged partial column ozone anomalies $\Delta \mathrm{PCO_{obs}}$ (line plots) for the different datasets and, for comparison, explained partial column ozone $\Delta \mathrm{PCO_{exp}}$ for ERA5 (area plots). See the text for details on the computation.

et al., 2022). Similar ozone response signatures can be observed during Eastern Pacific El Niño events (Benito-Barca et al., 2022, see, e. g., their Fig. 1g). They have furthermore been obtained from modern CMIP6 climate projections based on various climate forcing scenarios (Match and Gerber, 2022, e. g., their Fig. 1).

Finally, Figures 8(a–c) provide maps of the sample standard deviation derived from linearly detrended year-by-year variations of DJF ozone volume mixing ratios, which can be used to assess the local strength of interannual ozone variability for the different datasets used in this work. Given the clear similarities with the structure of the T100 regression maps from Fig. 3, we may ask to what extent polar vortex co-variability in general allows us to constrain polar ozone anomalies during northern hemispheric winters. To do so, we consider seasonal-mean ozone for DJF from ERAI, MLS and ERA5, each interpolated on equidistant pressure levels between 1 hPa and 300 hPa with 1 hPa vertical resolution and adjusted for linear trends across the corresponding time intervals. The observed variability of polar-cap averaged partial column ozone (PCO) then reads

$$\Delta \mathrm{PCO_{obs}}(t) = \left\langle \int_{1\,\mathrm{hPa}}^{300\,\mathrm{hPa}} \delta \overline{\chi}(t,p,\phi)\,\mathrm{d}p \right\rangle_{\phi \geq 60°\mathrm{N}}. \tag{5}$$

Based on the associated T100 regression map for ozone in the latitude-pressure plane, we reconstruct the variations that are explained by co-variability with the polar vortex,

$$\Delta \mathrm{PCO_{exp}}(t) = \overline{T}_{100}(t) \cdot \left\langle \int_{1\,\mathrm{hPa}}^{300\,\mathrm{hPa}} b(p,\phi)\,\mathrm{d}p \right\rangle_{\phi \geq 60°\mathrm{N}}, \tag{6}$$

Table 1. Variances of observed polar-cap averaged partial column ozone, ΔPCO_{obs} defined in eq. (5), explained by interannual variability of PCO_{exp} from eq. (6) associated with T100 anomalies. This table extends the results presented in Fig. 8. Explained variances are provided as the squared correlation coefficients obtained from least-squares linear regressions, where minimum and maximum values were derived from the corresponding 95 % confidence intervals for the correlation coefficients based on Fisher's z-transformation.

Dataset	Time range	Explained variance [%]		
		min	r^2	max
ERAI	1980–2016	28	53	72
ERA5		48	69	83
	1960–1980	21	55	79
	1980–2022	53	71	83
	2005–2020	47	78	92
MLS		63	86	95

corresponding to the general T100 index time series modulated by a constant prefactor that depends on the individual model
235 realisation. Finally, the correlation between these two PCO anomaly time series provides a measure for the variance of ΔPCO_{obs}
that is associated with seasonal polar vortex strength anomalies. The results obtained for ERAI, MLS and ERA5 are shown
in Fig. 8(d) and Table 1, which are based on the extended T100 index from ERA5. For a comprehensive analysis we added
separate computations for pre-satellite ERA5 data covering DJF 1960–1980.

Table 1 suggests that around 86 % of polar-cap averaged PCO variations from MLS are related with T100 co-variability.
240 This significantly differs from ERAI, where only slightly more than half of the variability can be attributed. Explained variances for ERA5 starting from DJF 1980 turn out to be substantially higher compared with ERAI and furthermore approach
the performance of MLS. The low value for the pre-satellite era in ERA5 suggests that more recent years in reanalyses are
much better constrained by observational data. However, it is unclear whether the remaining differences only result from the
individual model implementations, assimilation schemes and the quality of the measurements. Instead, e. g., given the growing
245 explained variances for ERA5 with time, the findings may also suggest a much more fundamental change in the interactions
between ozone and large-scale atmospheric dynamics. For example, Calvo et al. (2015) showed that stratospheric zonal wind
and temperature anomalies during Arctic ozone extremes occurred mainly in recent decades due to substantial anthropogenic
ozone depleting substances, indicating that ozone chemistry became increasingly important in governing climate variability.

To sum up, we showed that most of the interannual anomalies of polar column ozone in recent years can be attributed to wave-
250 driven anomalous dynamics associated with the varying strength of the polar vortex. The knowledge on the mechanisms that
constrain these leading modes of intrinsic ozone variability may help to understand long-term trends in response to external

forcings, i. e., due to evolving concentrations of ozone depleting substances or increased greenhouse gas emissions. (e. g., SPARC/IO3C/GAW, 2019) Moreover, feedbacks between anthropogenic climate change and stratospheric dynamics may cause modifications to these modes of variability. Exploring the extent to which ozone itself is involved here would be worth a closer
255 look.

Data availability. ERA-Interim data were provided by ECMWF through NCAR. They can be downloaded also from https://apps.ecmwf.int/datasets/data/interim-full-daily. Aura MLS version 5 data are available at https://mls.jpl.nasa.gov. Hersbach et al. (2019) was downloaded from the Copernicus Climate Change Service (C3S) Climate Data Store. Our study contains modified Copernicus Climate Change Service information 2023. Neither the European Commission nor ECMWF is responsible for any use that may be made of the Copernicus information
260 or data it contains.

Author contributions. FH performed the analyses, supervised by HG and TB. TB initiated the project and processed the ERA-Interim reanalyses. FP provided the MLS observational data. FH wrote the first draft of the paper. All authors contributed in interpreting the results and improving the manuscript.

Competing interests. The authors declare that they have no conflict of interest.

265 *Acknowledgements.* We thank Y. Desille for research on polar vortex–ozone co-variability from modern reanalyses and H. von Heydebrand for extending these studies to chemistry–climate models. We further thank the MLS team for providing the ozone satellite observation data. FH appreciates helpful suggestions by E. Gerber. This work was funded by the Deutsche Forschungsgemeinschaft (DFG, German Research Foundation) – TRR 301 – Project-ID 428312742: "The tropopause region in a changing atmosphere". Throughout this study, we used color codings based on ColorBrewer 2.0 (Brewer, 2022) and Scientific Colour Maps (Crameri et al., 2020; Crameri, 2022). We appreciate the
270 features provided by xarray (Hoyer and Hamman, 2017; Hoyer et al., 2022) and ProPlot (Davis, 2022).

References

Adam, O., Grise, K. M., Staten, P., Simpson, I. R., Davis, S. M., Davis, N. A., Waugh, D. W., Birner, T., and Ming, A.: The TropD software package (v1): standardized methods for calculating tropical-width diagnostics, Geosci. Model Dev., 11, 4339–4357, https://doi.org/10.5194/gmd-11-4339-2018, 2018.

Albers, J. R., Perlwitz, J., Butler, A. H., Birner, T., Kiladis, G. N., Lawrence, Z. D., Manney, G. L., Langford, A. O., and Dias, J.: Mechanisms governing interannual variability of stratosphere-to-troposphere ozone transport, J. Geophys. Res.-Atmos., 123, 234–260, https://doi.org/10.1002/2017JD026890, 2018.

Andrews, D. G., Holton, J. R., and Leovy, C. B.: Middle atmosphere dynamics, vol. 40 of *International Geophysics*, Academic Press, 1987.

Bahramvash Shams, S., Walden, V. P., Hannigan, J. W., Randel, W. J., Petropavlovskikh, I. V., Butler, A. H., and de la Cámara, A.: Analyzing ozone variations and uncertainties at high latitudes during sudden stratospheric warming events using MERRA-2, Atmos. Chem. Phys., 22, 5435–5458, https://doi.org/10.5194/acp-22-5435-2022, 2022.

Baldwin, M. P., Birner, T., Brasseur, G., Burrows, J., Butchart, N., Garcia, R., Geller, M., Gray, L., Hamilton, K., Harnik, N., Hegglin, M. I., Langematz, U., Robock, A., Sato, K., and Scaife, A. A.: 100 years of progress in understanding the stratosphere and mesosphere, Meteor. Mon., 59, 27.1–27.62, https://doi.org/10.1175/AMSMONOGRAPHS-D-19-0003.1, 2019.

Baldwin, M. P., Ayarzagüena, B., Birner, T., Butchart, N., Butler, A. H., Charlton-Perez, A. J., Domeisen, D. I. V., Garfinkel, C. I., Garny, H., Gerber, E. P., Hegglin, M. I., Langematz, U., and Pedatella, N. M.: Sudden stratospheric warmings, Rev. Geophys., 59, https://doi.org/10.1029/2020RG000708, 2021.

Bandoro, J., Solomon, S., Donohoe, A., Thompson, D. W. J., and Santer, B. D.: Influences of the Antarctic ozone hole on southern hemispheric summer climate change, J. Climate, 27, 6245–6264, https://doi.org/10.1175/JCLI-D-13-00698.1, 2014.

Barnes, P. W., Robson, T. M., Neale, P. J., Williamson, C. E., Zepp, R. G., Madronich, S., Wilson, S. R., Andrady, A. L., Heikkilä, A. M., Bernhard, G. H., Bais, A. F., Neale, R. E., Bornman, J. F., Jansen, M. A. K., Klekociuk, A. R., Martinez-Abaigar, J., Robinson, S. A., Wang, Q.-W., Banaszak, A. T., Häder, D.-P., Hylander, S., Rose, K. C., Wängberg, S.-Å., Foereid, B., Hou, W.-C., Ossola, R., Paul, N. D., Ukpebor, J. E., Andersen, M. P. S., Longstreth, J., Schikowski, T., Solomon, K. R., Sulzberger, B., Bruckman, L. S., Pandey, K. K., White, C. C., Zhu, L., Zhu, M., Aucamp, P. J., Liley, J. B., McKenzie, R. L., Berwick, M., Byrne, S. N., Hollestein, L. M., Lucas, R. M., Olsen, C. M., Rhodes, L. E., Yazar, S., and Young, A. R.: Environmental effects of stratospheric ozone depletion, UV radiation, and interactions with climate change: UNEP Environmental Effects Assessment Panel, Update 2021, Photochem. Photobiol. Sci., 21, 275–301, https://doi.org/10.1007/s43630-022-00176-5, 2022.

Bell, B., Hersbach, H., Simmons, A., Berrisford, P., Dahlgren, P., Horányi, A., Muñoz-Sabater, J., Nicolas, J., Radu, R., Schepers, D., Soci, C., Villaume, S., Bidlot, J.-R., Haimberger, L., Woollen, J., Buontempo, C., and Thépaut, J.-N.: The ERA5 global reanalysis: preliminary extension to 1950, Q. J. R. Meteorol. Soc., 147, 4186–4227, https://doi.org/10.1002/qj.4174, 2021.

Benito-Barca, S., Calvo, N., and Abalos, M.: Driving mechanisms for the El Niño–Southern Oscillation impact on stratospheric ozone, Atmos. Chem. Phys., 22, 15 729–15 745, https://doi.org/10.5194/acp-22-15729-2022, 2022.

Brasseur, G. P. and Solomon, S.: Aeronomy of the middle atmosphere. Chemistry and physics of the stratosphere and mesosphere, Springer Dordrecht, 3rd edn., 2005.

Brewer, C. A.: ColorBrewer 2.0, https://colorbrewer2.org, 2022.

Butchart, N.: The Brewer-Dobson circulation, Rev. Geophys., 52, 157–184, https://doi.org/10.1002/2013RG000448, 2014.

Butler, A. H., Sjoberg, J. P., Seidel, D. J., and Rosenlof, K. H.: A sudden stratospheric warming compendium, Earth Syst. Sci. Data, 9, 63–76, https://doi.org/10.5194/essd-9-63-2017, 2017.

Calvo, N., Polvani, L. M., and Solomon, S.: On the surface impact of Arctic stratospheric ozone extremes, Environ. Res. Lett., 10, https://doi.org/10.1088/1748-9326/10/9/094003, 2015.

Chiodo, G. and Polvani, L. M.: Reduced southern hemispheric circulation response to quadrupled CO_2 due to stratospheric ozone feedback, Geophys. Res. Lett., 44, 465–474, https://doi.org/10.1002/2016GL071011, 2017.

Chiodo, G. and Polvani, L. M.: The response of the ozone layer to quadrupled CO_2 concentrations: implications for climate, J. Climate, 32, 7629–7642, https://doi.org/10.1175/JCLI-D-19-0086.1, 2019.

Chiodo, G., Polvani, L. M., Marsh, D. R., Stenke, A., Ball, W., Rozanov, E., Muthers, S., and Tsigaridis, K.: The response of the ozone layer to quadrupled CO_2 concentrations, J. Climate, 31, 3893–3907, https://doi.org/10.1175/JCLI-D-17-0492.1, 2018.

Crameri, F.: Scientific colour maps, Zenodo [code], https://doi.org/10.5281/zenodo.1243862, 2022.

Crameri, F., Shephard, G. E., and Heron, P. J.: The misuse of colour in science communication, Nat. Commun., 11, https://doi.org/10.1038/s41467-020-19160-7, 2020.

Davis, L. L. B.: ProPlot, Zenodo [code], https://doi.org/10.5281/zenodo.3873878, 2022.

Davis, S. M., Hegglin, M. I., Dragani, R., Fujiwara, M., Harada, Y., Kobayashi, C., Long, C., Manney, G. L., Nash, E. R., Potter, G. L., Tegtmeier, S., Wang, T., Wargan, K., and Wright, J. S.: Overview of ozone and water vapour, in: SPARC Reanalysis Intercomparison Project (S-RIP) Final Report, edited by Fujiwara, M., Manney, G. L., Gray, L. J., and Wright, J. S., pp. 123–164, SPARC Report No. 10, WCRP-6/2021, https://doi.org/10.17874/800dee57d13, 2022.

de la Cámara, A., Abalos, M., and Hitchcock, P.: Changes in stratospheric transport and mixing during sudden stratospheric warmings, J. Geophys. Res.-Atmos., 123, 3356–3373, https://doi.org/10.1002/2017JD028007, 2018a.

de la Cámara, A., Abalos, M., Hitchcock, P., Calvo, N., and Garcia, R. R.: Response of Arctic ozone to sudden stratospheric warmings, Atmos. Chem. Phys., 18, 16 499–16 513, https://doi.org/10.5194/acp-18-16499-2018, 2018b.

Dee, D. P., Uppala, S. M., Simmons, A. J., Berrisford, P., Poli, P., Kobayashi, S., Andrae, U., Balmaseda, M. A., Balsamo, G., Bauer, P., Bechtold, P., Beljaars, A. C. M., van de Berg, L., Bidlot, J., Bormann, N., Delsol, C., Dragani, R., Fuentes, M., Geer, A. J., Haimberger, L., Healy, S. B., Hersbach, H., Hólm, E. V., Isaksen, L., Kållberg, P., Köhler, M., Matricardi, M., McNally, A. P., Monge-Sanz, B. M., Morcrette, J.-J., Park, B.-K., Peubey, C., de Rosnay, P., Tavolato, C., Thépaut, J.-N., and Vitart, F.: The ERA-Interim reanalysis: configuration and performance of the data assimiliation system, Q. J. R. Meteorol. Soc., 137, 553–597, https://doi.org/10.1002/qj.828, 2011.

Dietmüller, S., Ponater, M., and Sausen, R.: Interactive ozone induces a negative feedback in CO_2-driven climate change simulations, J. Geophys. Res.-Atmos., 119, 1796–1805, https://doi.org/10.1002/2013JD020575, 2014.

Domeisen, D. I. V., Butler, A. H., Charlton-Perez, A. J., Ayarzagüena, B., Baldwin, M. P., Dunn-Sigouin, E., Furtado, J. C., Garfinkel, C. I., Hitchcock, P., Karpechko, A. Y., Kim, H., Knight, J., Lang, A. L., Lim, E.-P., Marshall, A., Roff, G., Schwartz, C., Simpson, I. R., Son, S.-W., and Taguchi, M.: The role of the stratosphere in subseasonal to seasonal prediction: 2. Predictability arising from stratosphere-troposphere coupling, J. Geophys. Res.-Atmos., 125, https://doi.org/10.1029/2019JD030923, 2020.

Dragani, R.: On the quality of the ERA-Interim ozone reanalyses: comparisons with satellite data, Q. J. R. Meteorol. Soc., 137, 1312–1326, https://doi.org/10.1002/qj.821, 2011.

Friedel, M., Chiodo, G., Stenke, A., Domeisen, D. I. V., Fueglistaler, S., Anet, J. G., and Peter, T.: Springtime Arctic ozone depletion forces northern hemisphere climate anomalies, Nat. Geosci., 15, 541–547, https://doi.org/10.1038/s41561-022-00974-7, 2022a.

Friedel, M., Chiodo, G., Stenke, A., Domeisen, D. I. V., and Peter, T.: Effects of Arctic ozone on the stratospheric spring onset and its surface
345   impact, Atmos. Chem. Phys., 22, 13 997–14 017, https://doi.org/10.5194/acp-22-13997-2022, 2022b.

Fu, Q., Solomon, S., and Lin, P.: On the seasonal dependence of tropical lower-stratospheric temperature trends, Atmos. Chem. Phys., 10,
2643–2653, https://doi.org/10.5194/acp-10-2643-2010, 2010.

Gettelman, A., Hoor, P., Pan, L. L., Randel, W. J., Hegglin, M. I., and Birner, T.: The extratropical upper troposphere and lower stratosphere,
Rev. Geophys., 49, https://doi.org/10.1029/2011RG000355, 2011.

350   Grise, K. M., Thompson, D. W. J., and Birner, T.: A global survey of static stability in the stratosphere and upper troposphere, J. Climate, 23,
2275–2292, https://doi.org/10.1175/2009JCLI3369.1, 2010.

Haynes, P. H., McIntyre, M. E., Shepherd, T. G., Marks, C. J., and Shine, K. P.: On the "downward control" of extra-
tropical diabatic circulations by eddy-induced mean zonal forces, J. Atmos. Sci., 48, 651–678, https://doi.org/10.1175/1520-
0469(1991)048%3C0651:OTCOED%3E2.0.CO;2, 1991.

355   Hersbach, H., Bell, B., Berrisford, P., Biavati, G., Horányi, A., Muñoz-Sabater, J., Nicolas, J., Peubey, C., Radu, R., Rozum, I., Schepers, D.,
Simmons, A., Soci, C., Dee, D., and Thépaut, J.-N.: ERA5 monthly averaged data on pressure levels from 1959 to present, Copernicus
Climate Change Service (C3S) Climate Data Store (CDS), https://doi.org/10.24381/cds.6860a573, (accessed on 12 January 2023), 2019.

Hersbach, H., Bell, B., Berrisford, P., Hirahara, S., Horányi, A., Muñoz-Sabater, J., Nicolas, J., Peubey, C., Radu, R., Schepers, D., Simmons,
A., Soci, C., Abdalla, S., Abellan, X., Balsamo, G., Bechtold, P., Biavati, G., Bidlot, J., Bonavita, M., de Chiara, G., Dahlgren, P., Dee,
360   D., Diamantakis, M., Dragani, R., Flemming, J., Forbes, R., Fuentes, M., Geer, A., Haimberger, L., Healy, S., Hogan, R. J., Hólm, E.,
Janisková, M., Keeley, S., Laloyaux, P., Lopez, P., Lupu, C., Radnoti, G., de Rosnay, P., Rozum, I., Vamborg, F., Villaume, S., and Thépaut,
J.-N.: The ERA5 global reanalysis, Q. J. R. Meteorol. Soc., 146, 1999–2049, https://doi.org/10.1002/qj.3803, 2020.

Hitchcock, P., Shepherd, T. G., and Yoden, S.: On the approximation of local and linear radiative damping in the middle atmosphere, J.
Atmos. Sci., 67, 2070–2085, https://doi.org/10.1175/2009JAS3286.1, 2010.

365   Holton, J. R., Haynes, P. H., McIntyre, M. E., Douglass, A. R., Rood, R. B., and Pfister, L.: Stratosphere-troposphere exchange, Rev.
Geophys., 33, 403–439, https://doi.org/10.1029/95RG02097, 1995.

Hong, H.-J. and Reichler, T.: Local and remote response of ozone to Arctic stratospheric circulation extremes, Atmos. Chem. Phys., 21,
1159–1171, https://doi.org/10.5194/acp-21-1159-2021, 2021.

Hoyer, S. and Hamman, J. J.: xarray: N-D labeled arrays and datasets in Python, Journal of Open Research Software, 5,
370   https://doi.org/10.5334/jors.148, 2017.

Hoyer, S., Roos, M., Hamman, J., Magin, J., Cherian, D., Fitzgerald, C., Hauser, M., Fujii, K., Maussion, F., Imperiale, G., Clark, S., Kleeman,
A., Nicholas, T., Kluyver, T., Westling, J., Munroe, J., Amici, A., Barghini, A., Banihirwe, A., Bell, R., Hatfield-Dodds, Z., Abernathey, R.,
Bovy, B., Omotani, J., Mühlbauer, K., Roszko, M. K., and Wolfram, P. J.: xarray, Zenodo [code], https://doi.org/10.5281/zenodo.598201,
2022.

375   IPCC: Climate change 2021: The physical science basis: Contribution of working group I to the sixth assessment report of the Intergovern-
mental Panel on Climate Change, Cambridge University Press, [in press], 2021.

Ivy, D. J., Solomon, S., Calvo, N., and Thompson, D. W. J.: Observed connections of Arctic stratospheric ozone extremes to northern
hemisphere surface climate, Environ. Res. Lett., 12, https://doi.org/10.1088/1748-9326/aa57a4, 2017.

Konopka, P., Grooß, J.-U., Plöger, F., and Müller, R.: Annual cycle of horizontal in-mixing into the lower tropical stratosphere, J. Geophys.
380   Res., 114, https://doi.org/10.1029/2009JD011955, 2009.

Lait, L. R.: An alternative form for potential vorticity, J. Atmos. Sci., 51, 1754–1759, https://doi.org/10.1175/1520-0469(1994)051%3C1754:AAFFPV%3E2.0.CO;2, 1994.

Lawrence, Z. D., Perlwitz, J., Butler, A. H., Manney, G. L., Newman, P. A., Lee, S. H., and Nash, E. R.: The remarkably strong Arctic stratospheric polar vortex of winter 2020: links to record-breaking Arctic oscillation and ozone loss, J. Geophys. Res.-Atmos., 125, https://doi.org/10.1029/2020JD033271, 2020.

Livesey, N. J., Read, W. G., Wagner, P. A., Froidevaux, L., Santee, M. L., Schwartz, M. J., Lambert, A., Millán Valle, L. F., Pumphrey, H. C., Manney, G. L., Fuller, R. A., Jarnot, R. F., Knosp, B. W., and Lay, R. R.: Earth Observing System (EOS) Aura Microwave Limb Sounder (MLS) version 5.0x level 2 and 3 data quality and description document. Version 5.0–1.1a, JPL D-105336 Rev. B, https://mls.jpl.nasa.gov/data/v5-0_data_quality_document.pdf, 2022.

Lubis, S. W., Silverman, V., Matthes, K., Harnik, N., Omrani, N.-E., and Wahl, S.: How does downward planetary wave coupling affect polar stratospheric ozone in the Arctic winter stratosphere?, Atmos. Chem. Phys., 17, 2437–2458, https://doi.org/10.5194/acp-17-2437-2017, 2017.

Match, A. and Gerber, E. P.: Tropospheric expansion under global warming reduces tropical lower stratospheric ozone, Geophys. Res. Lett., https://doi.org/10.1029/2022GL099463, 2022.

Neu, J. L., Flury, T., Manney, G. L., Santee, M. L., Livesey, N. J., and Worden, J.: Tropospheric ozone variations governed by changes in stratospheric circulation, Nat. Geosci., 7, 340–344, https://doi.org/10.1038/ngeo2138, 2014.

Nowack, P. J., Abraham, N. L., Maycock, A. C., Braesicke, P., Gregory, J. M., Joshi, M. M., Osprey, A., and Pyle, J. A.: A large ozone-circulation feedback and its implications for global warming assessments, Nat. Clim. Change, 5, 41–45, https://doi.org/10.1038/nclimate2451, 2015.

Nowack, P. J., Abraham, N. L., Braesicke, P., and Pyle, J. A.: The impact of stratospheric ozone feedbacks on climate sensitivity estimates, J. Geophys. Res.-Atmos., 123, 4630–4641, https://doi.org/10.1002/2017JD027943, 2018.

Oehrlein, J., Chiodo, G., and Polvani, L. M.: The effect of interactive ozone chemistry on weak and strong stratospheric polar vortex events, Atmos. Chem. Phys., 20, 10 531–10 544, https://doi.org/10.5194/acp-20-10531-2020, 2020.

Plumb, R. A.: Stratospheric transport, J. Meteorol. Soc. Jpn. Ser. II, 80, 793–809, https://doi.org/10.2151/jmsj.80.793, 2002.

Smith, K. L. and Polvani, L. M.: The surface impacts of Arctic stratospheric ozone anomalies, Environ. Res. Lett., 9, https://doi.org/10.1088/1748-9326/9/7/074015, 2014.

Son, S.-W., Tandon, N. F., and Polvani, L. M.: The fine-scale structure of the global tropopause derived from COSMIC GPS radio occultation measurements, J. Geophys. Res.-Atmos., 116, https://doi.org/10.1029/2011JD016030, 2011.

Son, S.-W., Purich, A., Hendon, H. H., Kim, B.-M., and Polvani, L. M.: Improved seasonal forecast using ozone hole variability?, Geophys. Res. Lett., 40, 6231–6235, https://doi.org/10.1002/2013GL057731, 2013.

SPARC/IO3C/GAW: SPARC/IO3/GAW report on long-term ozone trends and uncertainties in the stratosphere: SPARC Report No. 9, GAW Report No. 241, WCRP-17/2018, https://doi.org/10.17874/f899e57a20b, 2019.

Tung, K. K.: Nongeostrophic theory of zonally averaged circulation. Part I: Formulation, J. Atmos. Sci., 43, 2600–2618, https://doi.org/10.1175/1520-0469(1986)043%3C2600:NTOZAC%3E2.0.CO;2, 1986.

von Heydebrand, H.: Interannual ozone variability in the Northern Hemisphere from coupled chemistry–climate models, Bachelor's thesis, Faculty of Physics, Ludwig-Maximilians-Universität, Munich, Germany, 2022.

Wang, M. and Fu, Q.: Stratosphere-troposphere exchange of air masses and ozone concentrations based on reanalyses and observations, J. Geophys. Res.-Atmos., 126, https://doi.org/10.1029/2021JD035159, 2021.

Wargan, K. and Coy, L.: Strengthening of the tropopause inversion layer during the 2009 sudden stratospheric warming: a MERRA-2 study,
420   J. Atmos. Sci., 73, 1871–1887, https://doi.org/10.1175/JAS-D-15-0333.1, 2016.

Waters, J. W., Froidevaux, L., Harwood, R. S., Jarnot, R. F., Pickett, H. M., Read, W. G., Siegel, P. H., Cofield, R. E., Filipiak, M. J., Flower,
    D. A., Holden, J. R., Lau, G. K., Livesey, N. J., Manney, G. L., Pumphrey, H. C., Santee, M. L., Wu, D. L., Cuddy, D. T., Lay, R. R.,
    Loo, M. S., Perun, V. S., Schwartz, M. J., Stek, P. C., Thurstans, R. P., Boyles, M. A., Chandra, K. M., Chavez, M. C., Chen, G.-S.,
    Chudasama, B. V., Dodge, R., Fuller, R. A., Girard, M. A., Jiang, J. H., Jiang, Y., Knosp, B. W., LaBelle, R. C., Lam, J. C., Lee, K. A.,
425   Miller, D., Oswald, J. E., Patel, N. C., Pukala, D. M., Quintero, O., Scaff, D. M., van Snyder, W., Tope, M. C., Wagner, P. A., and Walch,
    M. J.: The Earth observing system microwave limb sounder (EOS MLS) on the aura satellite, IEEE T. Geosci. Remote., 44, 1075–1092,
    https://doi.org/10.1109/TGRS.2006.873771, 2006.

Weber, M., Dikty, S., Burrows, J. P., Garny, H., Dameris, M., Kubin, A., Abalichin, J., and Langematz, U.: The Brewer-Dobson circulation
    and total ozone from seasonal to decadal time scales, Atmos. Chem. Phys., 11, 11 221–11 235, https://doi.org/10.5194/acp-11-11221-2011,
430   2011.

WMO: Meteorology – a three-dimensional science: Second session of the Commission for Aerology, WMO Bulletin, 6, 134–138, 1957.

WMO: Scientific assessment of ozone depletion: 2018: Global Ozone Research and Monitoring Project – Report No. 58, Geneva, 2018.

WMO: Executive Summary. Scientific Assessment of Ozone Depletion: 2022: GAW Report No. 278, Geneva, 2022.

Young, P. J., Rosenlof, K. H., Solomon, S., Sherwood, S. C., Fu, Q., and Lamarque, J.-F.: Changes in stratospheric temperatures and their im-
435   plications for changes in the Brewer-Dobson circulation, 1979–2005, J. Climate, 25, 1759–1772, https://doi.org/10.1175/2011JCLI4048.1,
    2012.